

Nanoscale

Accepted Manuscript



This is an *Accepted Manuscript*, which has been through the Royal Society of Chemistry peer review process and has been accepted for publication.

Accepted Manuscripts are published online shortly after acceptance, before technical editing, formatting and proof reading. Using this free service, authors can make their results available to the community, in citable form, before we publish the edited article. We will replace this *Accepted Manuscript* with the edited and formatted *Advance Article* as soon as it is available.

You can find more information about *Accepted Manuscripts* in the [Information for Authors](#).

Please note that technical editing may introduce minor changes to the text and/or graphics, which may alter content. The journal's standard [Terms & Conditions](#) and the [Ethical guidelines](#) still apply. In no event shall the Royal Society of Chemistry be held responsible for any errors or omissions in this *Accepted Manuscript* or any consequences arising from the use of any information it contains.

Cite this: DOI: 10.1039/c0xx00000x

www.rsc.org/xxxxxx

ARTICLE TYPE**Plasmonic Fano resonances in nanohole quadrumers for ultra-sensitive refractive index sensing**Yaohui Zhan,^{a†} Dang Yuan Lei^{bc†*}, Xiaofeng Li^{a*}, and Stefan A. Maier^d*Received (in XXX, XXX) XthXXXXXXXXXX 20XX, Accepted Xth XXXXXXXXXXXX 20XX*

DOI: 10.1039/b000000x

Plasmonic Fano resonances arising from electromagnetic interactions in metallic nanostructures exhibit spectral characteristics analogous to that from the electron waves in oligomer molecules. Though a great deal of research interests has been attracted to study the optical properties and explore the associated applications of metallic nanoparticle oligomers, the plasmonic response of their complementary structures – nanohole clusters remains largely unexplored. Here we show numerically by full-wave finite-element method that a nanohole quadramer can sustain two Fano resonances when the incident electric field is orientated along the long-axis of the quadramer system. The underlying physical mechanisms responsible for the Fano resonance formation are revealed explicitly by spectrally deconstructing the Fano lineshape, spatially decomposing the structure configuration and mapping the electric-field profile and charge distribution, which collectively demonstrate strong mode coupling between either two antiparallel dipolar modes or dipole-quadruple modes in the nanohole quadramer. We further show that the spectral profile of the Fano resonance including the resonance linewidth and spectral contrast can be engineered flexibly by adjusting the geometrical parameters of the nanohole cluster, including nanohole diameter, film thickness and interhole distance. With an optimized and realistic geometrical configuration, the nanohole quadramer system exhibits an overall sensing figure of merit up to 14.25, far surpassing the value reported for conventional nanoparticle oligomers.

1 Introduction

Plasmonic Fano resonances have become a research topic under intense investigation¹⁻³ due to their exotic characteristics such as the sharply asymmetrical lineshape, the extremely weak radiation damping⁴, and the high spectral sensitivity to changes in the local dielectric environment⁵. Fano resonances were originally proposed to explain theoretically the distinctively asymmetric absorption profile discovered in an atomic gas system⁶ and had been subsequently observed in many quantum systems. The intrinsic nature of a Fano resonance has been recognized as interference between the energy transferred from an initial state to a final state *via* two different pathways.⁵ In a plasmonic system, this corresponds to the interference between light energy directly coupled with a bright (superradiant) mode and that indirectly coupled with a dark (subradiant) mode *via* the near-field interaction with the bright mode; as a result, a sharp Fano dip arises as the dark and bright modes spectrally overlap but are excited out of phase.⁷ In other words, a Fano resonance in a complex metallic nanostructure can be decomposed into bright and dark modes sustained respectively by two subgroups of the whole system;⁸ these two types of modes hybridize and interfere with each other^{9,10}, resulting in an asymmetric Fano lineshape, in

close analogy to the spatial overlap of electron clouds around atomic and molecular orbitals¹¹⁻¹³. In the view of this analogy, many artificial plasmonic “molecules” have been proposed to generate pronounced Fano resonances, such as nanoshells,^{10,14} nanorods,¹⁵ nanotubes,¹⁶ theta-shaped structures,¹⁷ non-concentric ring/disk cavities,¹⁸ dolmen-like structures,^{18,19} and so forth. In particular, to mimic the formation of an oligomer molecule, metallic nanoparticles are self-assembled into nanoclusters including dimers,²⁰⁻²² trimers,²³ quadrumers,⁵ pentamers²⁴ and heptamers,²⁵⁻²⁹ which all support pronounced Fano dips. Furthermore, the Fano resonance lineshape including resonance linewidth and spectral contrast generated by these artificial molecules or oligomers can be tailored effectively by lowering the structure symmetry or tuning their geometric parameters.^{14,30,31}

The aforementioned fascinating properties associated with Fano resonances have enabled a variety of potential applications including chemical and biological sensors^{5,7,24}, optical switches³², photodetectors³³ and surface enhanced Raman scattering³⁴, etc. In particular, a great deal of efforts has been devoted to develop plasmonic Fano-resonance-based biosensors. This application mainly takes advantage of the extremely-low radiation damping at a Fano dip, which gives rises to a very narrow resonance linewidth and hence increases the overall sensing figure of merit

(FoM) as well as the detection resolution. So far, the highest sensing FoM predicted with Fano resonances is 8.34 for a nonconcentric ring-disk cavity structure³⁵ while the highest value achieved in experiment is 5.7 for a heptamer cluster³⁰ and 6.7 for a quadrumer cluster⁵. Obviously, such values of FoM are not comparable with that achieved for propagating surface plasmon resonances excited in periodic nanohole³⁶, nanoparticle arrays^{37,38,39}, individual nanorice/nanobelts⁴⁰ or with that demonstrated for hybrid plasmonic-photonic modes^{41,42} in more complex systems. There is still much room to improve the overall sensing performance of plasmonic oligomers-based refractive index sensors, with an ultimate aim of detecting a tiny change in the local environment like the single-molecule adsorption event.

Different from previous studies focusing mainly on plasmonic Fano resonances sustained by complex metallic nanoparticles, here we demonstrate numerically for the first time the existence of pronounced Fano resonances in a nanohole quadrumer drilled in a metal film – a structure counterpart complementary to the well-studied nanoparticle quadrumer. To reveal the underlying physical mechanisms responsible for the formation of the Fano dips in the scattering spectrum of the nanohole cluster, we decompose the overall Fano lineshape into a pair of symmetric (bright) and asymmetric (dark) modes, which are associated with two subgroups of the whole system, respectively, as confirmed by the electric-field profile and charge distribution at each resonance. We further examine how the Fano profile is affected by nanohole cluster size and geometry. Most importantly, we find that such a nanohole quadrumer sitting on a non-transparent metal layer exhibits an overall bulk sensing FoM up to 14.25, which far surpasses the value achieved with the nanoparticle counterpart.

2 Results and discussions

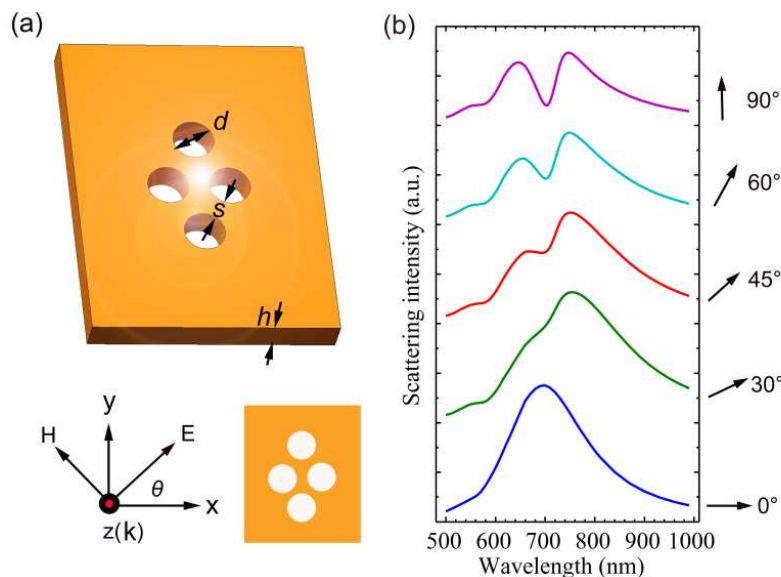


Fig. 1 (a) Schematic diagram of a quadrumer hole-cluster in a gold plate; (b) Evolution of the scattering response of the quadrumer hole-cluster at normal incidence illumination with different polarization angles, where the 0 (90) degree corresponds to the positive x (y) direction. The diameter of each hole d , interhole distance s , and the thickness of the Au plate h are initially taken to be 100 nm, 6 nm, and 30 nm, respectively.

The proposed nanohole quadrumer belongs to the D_{2h} group whose strong polarization dependence can be also ascribed to the

2.1 Polarization dependence and symmetry breaking

We begin our analysis by examining the scattering response of a symmetric nanohole quadrumer excited at normal incidence with different polarizations. As shown in Fig. 1(a), four holes with identical diameter d and interhole distance s are milled in a gold plate with thickness of h ; the orientation angle θ of the incident electric field relative to the short-axis of the nanohole cluster (i.e., x) is shown at the bottom. The evolution of the scattering response with θ is shown in Fig. 1(b). One can see that at $\theta = 0^\circ$ (i.e., E is polarized along x), the scattering spectrum shows a broad resonance with a single peak due to collective excitation of the electric dipoles in the four holes; at $\theta = 30^\circ$, two shallow scattering dips emerge respectively at wavelengths $\lambda \sim 580$ nm and 690 nm due to the presence of electric-field y -component E_y that creates a symmetry breaking to the whole system. Further increase of the polarization angle enhances E_y and subsequently induces a redshift of the scattering dips, which can be seen from the appearance of a prominent dip at $\lambda = 705$ nm for $\theta = 90^\circ$. As we will discuss later, the two scattering dips are due to the formation of Fano resonances resulting from the excited anti-bonding state and plasmon hybridization between resonances of different orders in the system. Consequently, the plasmon interaction in the nanohole cluster exhibits a strong dependence on the incident polarization, primarily due to the orientation-dependent capacitive coupling within the hole cluster.⁵ A potential application of this distinct polarization preference is to implant such a Fano structure into a liquid crystal device and switch the Fano dip on and off in a voltage-controlled manner.⁸ Because of this particular characteristic of nanohole clusters, the incident polarization angle $\theta = 90^\circ$ is chosen in the following studies.

reduced symmetry compared to D_{nh} ($n \geq 3$) groups with polarization independence already proven by Hopkins et al. based

on particle systems⁴³. To further examine this property, the sensitivity of the scattering response on the geometrical symmetry is investigated. As shown in Inset of Fig. 2(b), to transform the symmetry of the nanohole quadrumer from D_{2h} to D_{4h} , the interhole distance along the short-axis (x-axis) is stretched gradually by Δ with other parameters remaining unchanged. The scattering spectra as function of Δ are given in Fig. 2(a), which display a strong dependence of Fano resonance on the geometrical symmetry. As Δ is increased slightly by 6 nm, the long-wavelength Fano dip blue-shifts largely and damps dramatically. Increasing Δ further, both dips get shallower at $\Delta = 22$ nm and finally become undistinguishable and 78 nm. Note that, at $\Delta = 22$ nm, the nanoholes can be reorganized as a circular ring, i.e., having a D_{4h} group symmetry. We then investigate the polarization dependence of the nanohole quadrumer with the D_{4h} group in Fig. 2(b), which shows that the scattering response of this symmetric system exhibits polarization independence. This suggests that the conclusion of polarization independence in systems with D_{4h} symmetry is valid not only for nanoparticle oligomers but also for nanohole clusters. In addition, a weak but perceivable Fano dip is sustained persistently in the D_{4h} nanoholes, which agrees well with the previous work by Hopkins et al^{43,44}. At last, the analysis points out the necessity of reducing the symmetry of quadrumers from D_{4h} to D_{2h} in order to generate a prominent Fano resonance.

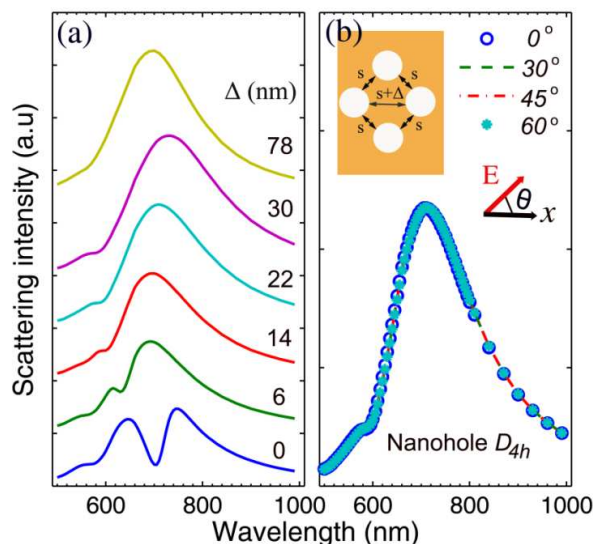


Fig. 2 (a) Scattering spectra as a function of Δ , a parameter defining the degree of symmetry in the nanohole quadrumer, i.e. the interhole distance along x-axis as shown in the inset of (b); (b) Scattering response of the nanohole quadrumer with D_{4h} symmetry as a function of the incidence polarization under normal incidence.

2.2 Spectral and subgroup decomposition of Fano resonances

To interpret quantitatively the scattering properties shown in Fig. 1(b), it is necessary to decompose mathematically the hybridized Fano lineshape into two standard subspectra, one with symmetric profile and the other with asymmetric profile. For this purpose, a few mathematical models have been built up delicately based on the physical generation mechanisms of Fano resonances^{4,20,45-47} in many coupled systems. Considering the complex electric permittivity of metals in plasmonic systems, however, both the

mass oscillator model proposed by many researchers and the quantum mechanical theory by Ugo Fano are not sufficient to provide a complete scenario of plasmonic Fano resonances. To resolve this problem, Gallinet and Martin derived a closed-form analytical formula based on *ab initio* theory to reveal the roles played by the electromagnetic modes and material losses in the metallic nanostructures.⁸ The measurable resonance magnitude in the entire system is given by the product of symmetric and asymmetric resonances which correspond to the bright and dark modes, respectively:

$$\sigma_{total}(\omega) = \prod_{i,j=1}^n \sigma_a^i(\omega) \sigma_s^j(\omega) \quad (1)$$

where the superscript $i(j) = 1, 2, 3, \dots, n$, indicates the decomposed i th (j th) asymmetric (symmetric) subspectrum σ_a (σ_s). σ_a and σ_s can be expressed as:⁸

$$\sigma_a^i(\omega) = \frac{[(\omega^2 - \omega_{ia}^2)/(2W_{ia}\omega_{ia}) + q_i]^2 + b_i}{[(\omega^2 - \omega_{ia}^2)/(2W_{ia}\omega_{ia})]^2 + 1} \quad (2)$$

$$\sigma_s^j(\omega) = \frac{a_j^2}{[(\omega^2 - \omega_{js}^2)/(2W_{js}\omega_{js})]^2 + 1} \quad (3)$$

where ω is the frequency, ω_a (ω_s) the central frequency of the dark (bright) mode resonance, W_a (W_s) the spectral linewidth of the asymmetric (symmetric) subspectrum, a the relative amplitude of the resonance, q the asymmetry factor, and b the damping coefficient proportional to the intrinsic loss.

The subspectra decomposed for the nanohole quadrumer are shown in Fig. 3(c), along with the scattering spectra for a nanohole dimer (Fig. 3(a)) and a nanohole trimer (Fig. 3(b)). All the nanohole clusters have an identical interhole distance (6 nm), diameter (100 nm) and plate thickness (30 nm) for direct comparison. Because direct analysis on the decomposition results of the nanohole quadrumer turns out to be very complicated, we start our discussions with the two simple systems, i.e. nanohole dimer and trimer. As shown in Fig. 3(a), the scattering spectrum of the nanohole dimer exhibits a broad resonance peaked at approximately 715 nm, which is due to excitations of the two electric dipole resonances in both nanoholes as confirmed later by their near-field distribution profiles and the charge plots. Upon the formation of a nanohole trimer by adding a third nanohole on top of the dimer, a shallow dip emerges in the scattering spectrum at wavelength 585 nm as shown in Fig. 3(b), resulting in an overall Fano lineshape. This weak Fano profile can be decomposed into a symmetric, broad resonance (red line) and an asymmetric, narrow one (grey line), the product of which two (blue line) produces exactly the original spectrum (open circles). From the detailed fit with Eq. 1, we derive for the Fano dip a central frequency $\omega_a = 2.12$ eV (585 nm) and an asymmetric parameter $q = 0.256$ (see Table 1). As for the nanohole quadrumer, in addition to the shallow Fano dip centred at wavelength 585 nm inherited from the trimer, a pronounced scattering dip appears at wavelength 700 nm. A similar mathematical fit reveals that this strong Fano dip is a consequence of the interaction between a bright mode peaked at

661 nm ($\omega_a = 1.876$ eV) and a dark mode centred at 723 nm ($\omega_a = 1.715$ eV). In the meantime, the weak Fano resonance at the short wavelength range can be decomposed into the same bright mode and another dark mode centred at 585 nm ($\omega_a = 2.12$ eV). This way the complex spectral profile for the nanohole quadrumer can be precisely reproduced as the product of one bright mode and two dark modes. All the fitting parameters extracted for the trimer and quadrumer nanohole clusters are listed in Table 1 for a more quantitative understanding on the Fano spectral profile. As the structure evolves from a nanohole trimer to a nanohole quadrumer, both the spectral linewidths of Fano I (W_a) and the bright mode (W_s) are broadened by ~ 0.02 eV,

suggesting slightly increased radiative and nonradiative damping.⁵ The parameter b for Fano I is much greater (~ 0.3 eV) than Fano II, which indicates a huge intrinsic loss associated with the dark mode occurring at the high energy and thus explains the observation that the dip at wavelength 585 nm (2.12 eV) is much shallower than that centred at wavelength 723 nm (1.715 eV). In addition, the asymmetrical factors q for Fano dips I and II are opposite in sign, which indicates that their higher scattering amplitudes are located respectively at the high- and low-energy frequency ranges with respect to the central frequency of the bright mode.

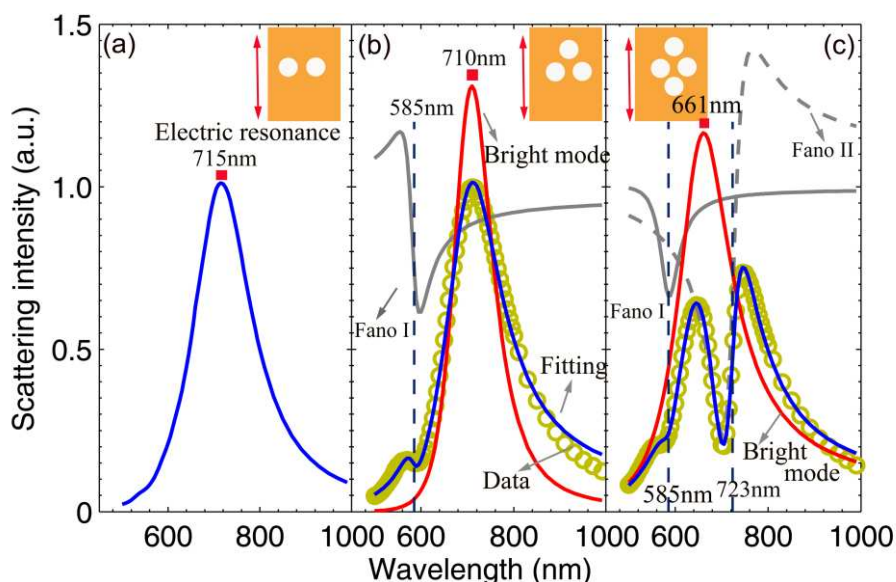


Fig. 3 Scattering spectra for (a) a nanohole dimer, (b) a nanohole trimer (open circles), and (c) a nanohole quadrumer (open circles) with $d = 100$ nm, $s = 6$ nm and $h = 30$ nm. The scattering spectrum of the nanohole trimer (nanohole quadrumer) is decomposed into a symmetric line shape corresponding to a bright mode and an (two) asymmetric one(s) corresponding to a (two) dark mode(s). The product of the bright and the dark modes gives exactly the blue lines in (b) and (c) which coincide well with the simulated data. The vertical dash-lines indicate the central positions of the subpectra.

Table 1 Values of key parameters obtained by fitting the spectra in Fig. 3 with Eq. 1.

		ω_a (eV)	W_a (eV)	q	b	a	ω_s (eV)	W_s (eV)
Trimer	Fano I	2.120	0.074	0.256	0.714	1.070	1.746	0.187
	Fano II	2.120	0.089	0.030	0.662	1.079	1.876	0.203
Quadrumer	Fano I	1.715	0.071	-0.570	0.336	1.079	1.876	0.203
	Fano II	1.715	0.071	-0.570	0.336	1.079	1.876	0.203

The spectral decomposition analysis made above implies that the nanohole quadrumer can be decomposed into two subgroups, i.e. a nanohole dimer and a trimer that are constituents of the whole quadrumer system.^{48,49} Specifically, since the scattering peak of the nanohole dimer is very close to that of the derived bright modes for both the trimer and quadrumer, we can assign the dimer as a subgroup for the latter two systems; Since the Fano dip in the scattering spectrum of the trimer also appears for the quadrumer, we can assign the trimer as a subgroup of the nanohole quadrumer. This way we can deconstruct the complex quadrumer into two subgroups in which the dimer corresponds to the two central holes in the quadrumer and the trimer to the upper three holes or the bottom three ones due to the structural symmetry. Therefore, the first subgroup (dimer) is responsible for generating a bright mode in the quadrumer system and the second

subgroup (trimer) is responsible for creating two dark modes; the destructive interference between the bright mode and the two dark modes gives rise to the double Fano resonances. Such structure deconstruction will be revealed more explicitly by the electric near-field distributions and charge plots at the respective resonances.

2.3 Near-field and charge-density distributions revealing the formation mechanisms of Fano resonances

To get deeper insights into the underlying physical mechanisms responsible for the formation of Fano resonances in the nanohole quadrumer, the electric near-field profiles at respective spectral positions are obtained with three-dimensional (3D) full-wave simulations based on the Finite Element Method. From the electric field distribution, we calculate the charge density distribution by applying Gauss's law:

$$\rho = \epsilon_0 \nabla \cdot E \quad (4)$$

where E is the electric field vector in near field, ρ the charge density, and ϵ_0 the permittivity in vacuum. In our calculations, the electric field is evaluated at 1 nm above the nanohole surface.

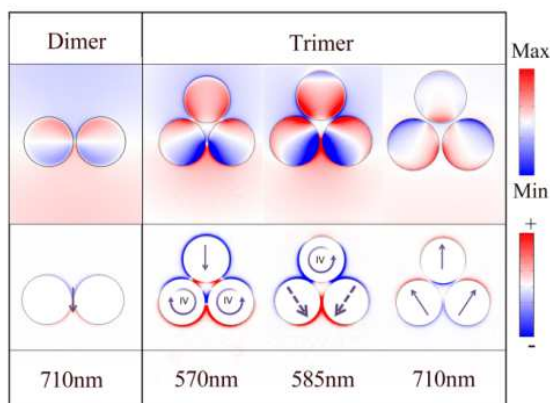


Fig. 4 Normalized E_z field and charge distribution at representative frequencies for the dimer and trimer hole clusters.

We still start from the dimer and trimer systems, and their near-field profiles and charge distribution are shown in Fig. 4. The upper row in the figure displays the profiles of the electric field along z (i.e., E_z) and the bottom row shows the charge

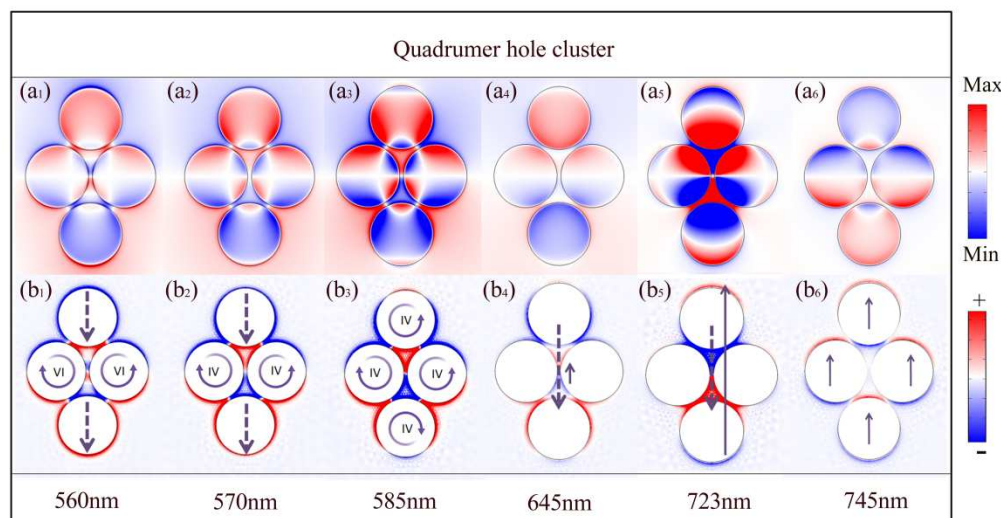


Fig. 5 (a₁)-(a₆) Normalized E_z profiles and (b₁)-(b₆) charge distributions at representative wavelengths. The diameter, interhole distance and plate thickness are exemplified as 100 nm, 6 nm and 30 nm, respectively.

We then proceed to the case of quadrumer holes, with their results shown in Fig. 5. The upper row in the figure displays the normalized E_z at the representative wavelengths and the lower row shows the corresponding charge density distributions. We observe a few higher-order modes in the high-energy region, for instance, two sextupole modes at 560 nm (Fig. 5(b₁)) and two quadrupole modes at 570 nm (Fig. 5(b₂)) excited in the two holes along x . However, these multipolar modes contribute little to the total moment due to their subradiant characters. Therefore, the dipolar modes in the top and bottom holes (along y) play a major role in determining the overall momentum of the system. When

density distributions with arrows indicating schematically the momentum direction. As seen in Fig. 4, a typical electric dipole is formed clearly in the dimer at $\lambda \sim 710$ nm; the dilute charge concentration and light-colored E_z profile reflect indirectly the superradiant nature of the dipolar mode. Such a dipolar mode can also be found in the trimer system at the same wavelength (e.g., $\lambda = 710$ nm), where all the dipole moments point consistently to the y -direction with the x -components completely cancelled out due to the structure symmetry. The in-phase coupling of these dipolar modes generates the strong scattering peak in Figs. 3(b), which always occurs in the low photon-energy region. In the high-energy region, higher order plasmonic modes can be excited. For instance, at $\lambda = 570$ nm, two quadrupolar moments appear distinctly in the two holes at the bottom, but contribute almost no dipole moment to the entire system. A direct consequence is that only the single dipolar mode excited in the top hole contributes to the total momentum and therefore forms the weak scattering peak as observed in Fig. 3(b). With lowering the incident photon energy, e.g., from $\lambda = 570$ nm to 585 nm, the two quadrupolar modes evolve into dipolar modes while the original dipolar mode in the upper hole becomes an imperfect quadrupolar mode, which exhibits a roughly upward dipole moment due to the asymmetric charge distribution. As the two dipolar modes couple into a net downward dipole moment, the hybridization of the top and bottom parts generates a subradiant mode, responsible for the shallow dip observed in Fig. 3(b).

the dipolar plasmon modes oscillate in phase, a lower spectral peak turns up (e.g., near 560 nm). As the sextupoles grow into quadrupoles, the scattering intensity increases gradually; especially, when the dipolar modes in the top and bottom holes also evolves as quadruple modes at 585 nm, a Fano dip “minimum” is formed (see Figs. 5(a₃) and 5(b₃)). In the lower photon-energy region, as plotted in Figs. 5(b₄)-(b₆), dipolar modes of different arrangements dominate the whole system. Due to the strong inter-mode coupling, the system is likely to exhibit either strong peaks or prominent dips under constructive or destructive interactions. Specifically, at 645nm as shown in Fig.

5(b₄), there are two dipolar modes, with the stronger one formed by the charges distributed at the upper and low parts of the system and the other weaker one at the central part. Although these two dipoles are in reverse directions, the external dipole is much stronger (due to the larger quantity of charges involved and longer separation distance) than the internal one, resulting in a peak in the scattering spectrum. However, at 723 nm, a pair of antiparallel dipole moments forming an antibonding, dark mode emerges as shown in Fig. 5(b₅). The destructive interaction between the two amplitude-comparable but reversely-orientated dipolar modes gives rise to the pronounced Fano II dip (see Fig. 3(c)). At 745nm, a typical binding, bright mode can be clearly seen in Fig. 5(b₆), with the four dipolar modes oscillating in phase and leading to the strongest peak (see Fig. 3(c)). We have to point out that even though the central frequency of the Fano lineshape is not located at the extreme point (maximum or minimum) of the total spectra, it corresponds exactly to the resonant excitation of the dark mode⁸.

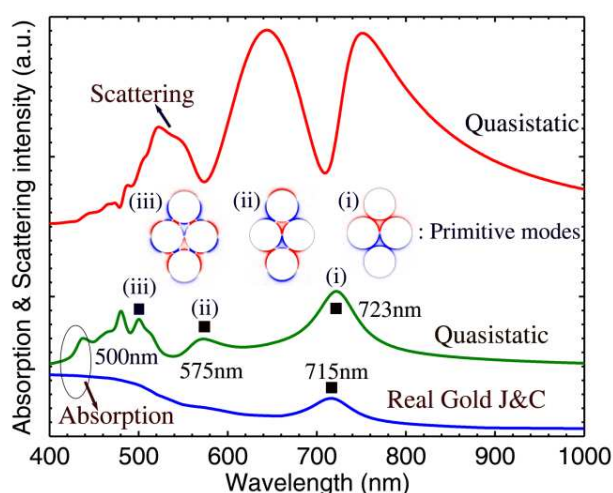
It's worth noting that the "dark" modes defined above are actually the "subradiant" modes, which means that they are not completely dark as they also include the excitable modes with comparatively low projection onto the incident field⁴⁴. Second, the theoretical framework based on "bright" and "dark" modes (as mentioned above and adopted in a large number of literatures^{5,7,10-31}) just takes into account the hybridized and approximate modes⁴⁴ in order to interpret the physical origin of Fano resonance, which are apparently different from the primitive and exact modes proposed by Hopkins et al⁴⁴. According to Hopkins et al, the interference of bright and dark (subradiant) modes is a sufficient but not necessary condition to generate a Fano resonance, because the interference between completely bright modes can also produce a resonance with Fano-like lineshape. However, under some specific configurations (e.g., the systems discussed in Refs. 5,7,10 etc. and this study), the methods based on bright-dark modes and the primitive modes are both effective to reconstruct the optical response or locate the near-field interference. In fact, they are two different approaches towards an identical destination in some special cases; despite so, the latter method based on primitive modes are more universal and can be utilized in 1) D_{nh} systems with n ($n \geq 3$) particles placed circularly in ring and 2) the all-dielectric systems without the participation of plasmonic oscillations⁴⁴. Therefore, the Fano resonance that can be interpreted by the bright-dark modes can also be dealt with by the primitive modes, but not vice versa. In the view of these observations, we make in the following additional analysis based on primitive modes to understand the resonance origin in the nanohole cluster system.

Our mode analysis is based on the quasi-electrostatic approximation, which has been widely used to investigate plasmonic systems^{50,51}. To simplify the analysis, the Drude model (DM) is employed to describe the dielectric response of Au⁵²

$$\varepsilon(\omega) = \varepsilon_{\infty} - \omega_p^2 / (\omega^2 + i\omega\Gamma) \quad (5)$$

with the Drude constant $\varepsilon_{\infty} = 9.5$, plasmon frequency $\omega_p = 8.95$ eV, damping frequency $\Gamma = 0.069$ eV.⁵³ This DM neglects the interband transitions above ~ 2.25 eV and otherwise provides an accurate parametrization of the experimental data of Au.⁵⁴ Under

quasistatic approximation, the absorption and scattering spectra of the same system shown in Fig. 1 are recalculated in Fig. 6, where the suppression of the scattering is always accompanied by the absorption enhancement⁵⁵. The absorption peaks locate at 723 nm (i), 575 nm (ii) and 500 nm (iii) respectively in the concerned spectral range ($500 \text{ nm} < \lambda < 1000 \text{ nm}$) at which the maxima of the near-field enhancement and localization occurs. More importantly, the absorption peaks are coincident well with the results (i.e., peak (i) at 723 nm and (ii) at 585 nm) in Fig. 3(c) obtained previously by spectral reconstructing. We have also calculated the absorption spectrum using the experimental data from Johnson & Christy (J&C) for Au (see the blue curve in Fig. 6). Compared to the result from quasistatic approximation, higher order modes (e.g., ii and iii) cannot be clearly found due to the large radiative damping. This explains the reason why an exact mode analysis can only be carried out under the electrostatic limit.⁵²



75 Fig. 6 Absorption (green) and scattering (red) spectra under quasistatic approximation. The absorption spectrum (blue) with experimental Au parameters (J&C) is also included for comparison. Inset: Primitive modes at representative spectral features.

According to Zhang et al⁵², the plasmonic modes at the absorption peaks correspond exactly to the real and primitive modes; these primitive modes are all bright modes if they are excited under an incident plane-wave instead of manual and anti-symmetric dark-mode excitation^{52,56}. Due to the complexity of the dark-mode excitation, we only get all the bright primitive modes in the system and compare them with the hybridized modes provided above, which is clear enough to examine the origin of Fano resonances further. As shown in the insets of Fig. 6, the primitive mode (i) at 723 nm is dipolar and superradiant; however, the corresponding hybridized mode shown in Fig. 5(b₅) exhibits an anti-bonding charge distribution, which suggests reversely that an unexcitable, dark mode must exist at this wavelength⁵². In addition, the primitive mode (ii) at 575 nm exhibits the same charge distribution as that from the corresponding hybridized mode in Fig. 5(b₃), which indicates that the Fano dip at 585 nm can be ascribed to the interference between the excitable subradiant, primitive mode (ii) and the tail of the overall dipolar mode. At last, the primitive mode (iii) at 500 nm, a mixture of sextupolar and octupolar modes, is

spectrally far from the concerned Fano dip and just manifests the excitability of even higher-order plasmonic modes.

2.4 Spectral tunability with geometric parameters

Engineering the spectral features by tuning geometric parameters is one of the most fascinating properties expected for artificial oligomers, which should be designed flexibly and effectively towards realizing targeted functionalities. In this section, the tunability of the pronounced Fano response by adjusting the characteristic dimensions of the quadramer nanohole cluster is investigated comprehensively. First, the spectral response as a function of the hole diameter ($50 < d < 300$ nm) is examined in

Fig. 7(a), where $h = 30$ nm and $s = 6$ nm. It is shown that the Fano response of nanohole quadramer can be tuned effectively by controlling the nanohole size. As d is as small as 50 nm, the spectral contrast is too weak to be identified, which can be improved by increasing d , suggesting a stronger plasmonic coupling effect in the nanohole cluster. In addition, as d increases, both the peaks and dips redshift accompanied by a significant spectral broadening. The wavelength shift for the second Fano dip can be over 500 nm (see the right-most black dash line in Fig. 7(a)), demonstrating excellent tunability of the Fano resonance by controlling nanohole diameter.

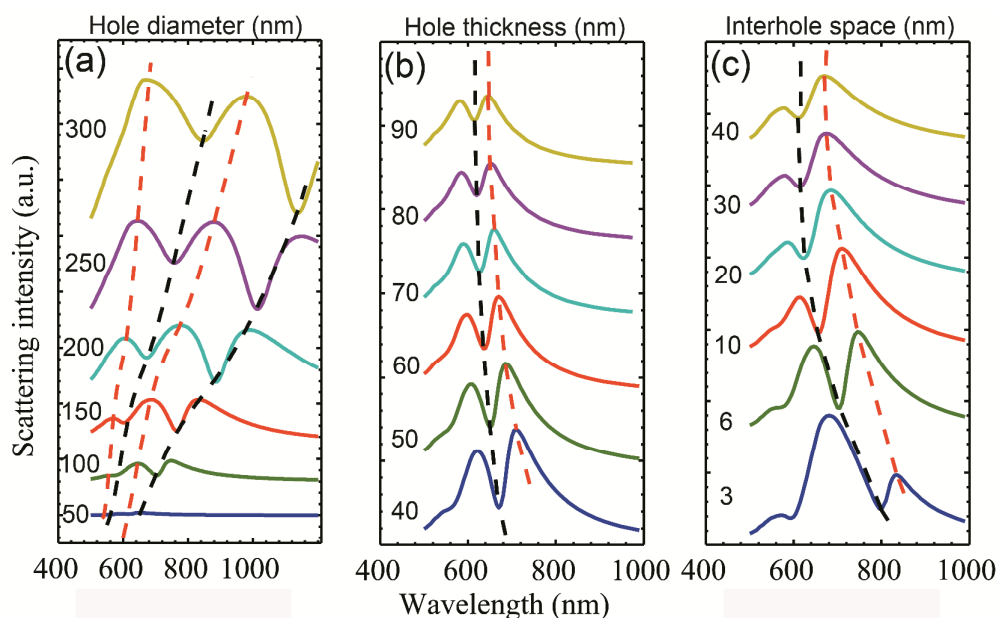


Fig. 7 Scattering spectra of the nanohole quadramer as a function of (a) hole diameter d ($s = 6$ nm and $h = 30$ nm), (b) plate thickness h ($d = 100$ nm and $h = 30$ nm), and (c) interhole distance s ($d = 100$ nm and $s = 6$ nm). The whole system stands alone in air under a y-polarized normal-incidence illumination. Dashed lines indicate the positions of the dark modes (black) and bright modes (brick red).

The Fano lineshape can be further refined by adjusting the thickness of the nanohole cluster h and the interhole distance s . As shown in Fig. 7(b), unlike the red-shift behaviour with increasing d , the superradiant and subradiant modes blue-shift slightly as h increases from 40 to 90 nm ($s = 6$ nm and $d = 100$ nm). In addition, the superradiant modes blue-shift more strongly than the subradiant modes, resulting in a narrowed scattering dip for nanoholes with larger depth. In the meanwhile, the spectral contrast of the Fano dip degrades with increasing h . Figure 7(c) presents the dependence of the Fano response on the interhole distance resonance blue-shift caused by increasing the interhole distance s . Interestingly, with increasing s , the scattering peaks in the long-wavelength region indicated by the red dashed line become stronger in intensity while the peaks on the left get weaker, indicating that the central position ω_s of the effective bright mode is red-shifted. In view of these observations, we can conclude that the nanohole quadramer system has excellent spectral tunability, including spectral contrast, resonance linewidth, frequency shift, resonance intensity and other subtle characteristics. This opens up a number of opportunities for applications where the sensitive spectral response against the system parameters and surrounding environment can be used.

2.5 Refractive index sensing studies

One of the most fascinating applications for nanohole clusters might be in ultra-sensitive biochemical sensing. The sensing performance of a plasmonic biosensor can be evaluated by the overall Figure of Merit (FoM), which is typically defined as the energy shift per unit refractive index change divided by the spectral linewidth, i.e., $(\Delta E/\Delta n)/\text{linewidth}$. It is noted that a simple full width at half maximum (FWHM) is no longer applicable for the definition of the resonance linewidth of an asymmetric lineshape associated with Fano resonances. A more accurate definition could be the energy difference between the Fano dip and its closest peak, according to the conventions used in previous literatures^{5,7,24}.

Considering the feasibilities of biosensing experiments, a nanohole quadramer supported by silica substrate is investigated with particular attention to the sensitivity when changing the refractive index of the local environment from 1.1 to 1.5. Based on previous discussions in section 2.4, an optimal structure (i.e., $d = 100$ nm, $s = 6$ nm, $h = 90$ nm) is adopted for the refractive index sensing application with selection criteria as follows. Although the spectral contrast improves advantageously as the nanohole diameter increases, the spectral linewidth is broadened

greatly due to the increased radiation damping, leading to a much lower FoM (Fig. 7(a)). Therefore, a smaller diameter, e.g., 100 nm, is favourable as long as the spectral contrast is not too low. For the plate thickness, a thicker one is preferred in order to

obtain a narrower linewidth (Fig. 7(b)). For the interhole distance, a moderate value of 6 nm is used since the spectral contrast between the dip and the closest peak is better than others (Fig. 7(c)).

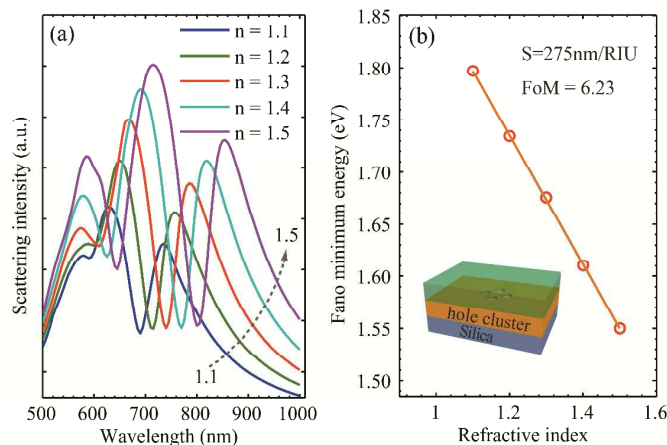


Fig. 8 (a) Scattering spectra for a nanohole quadrumer on silica as a function of the refractive index of the environment. The diameter, interhole distance and plate thickness are 100 nm, 6 nm and 90 nm, respectively. (b) Plot of the Fano dip position as a function of the refractive index (open circles). The solid line is a linear fit to the data points and its slope is defined as the sensitivity.

As shown in Fig. 8(a), the nanohole quadrumer immersed in the substance with $n = 1.1$ exhibits a Fano dip at 690 nm; with increasing n to 1.5, the dip shifts to 800 nm. Thus, the shift in wavelength per unit refractive index, noted as S , is calculated to be 275 nm/RIU for the current system. Figure 8(b) reveals a linear relationship between the dip position (in eV) and the refractive index with a slope of 0.618 eV/RIU. The averaged resonance linewidth of the Fano dips is calculated to be $\sim 0.098 \text{ eV}$. This results in an overall FoM of 6.23 for the nanohole quadrumer system, which is commensurate with the nanoparticle quadrumer (FoM = 6.7 in Ref. 5).

The FoM value can be further improved by replacing the

silica substrate with an Au/silica double layer as shown in Fig. 9. The thickness of the Au layer added is 40 nm, which is much larger than the skin depth of Au (3.3 nm in the visible range); therefore, a thicker Au layer does not noticeably modify the system response, enabling a better flexibility in fabrication. As shown in Fig. 9(a), increasing n from 1.1 to 1.5, the Fano dip shifts from 615 to 750 nm, giving rise to $S = 338 \text{ nm/RIU}$. The sensitivity in energy can be extracted from the slope in Fig. 9(b), 0.9073 eV/RIU. Together with an averaged resonance linewidth of 0.0637 eV, the overall FoM is now boosted up to 14.25, which is 2.13 times larger than that from the nanoparticle counterpart.

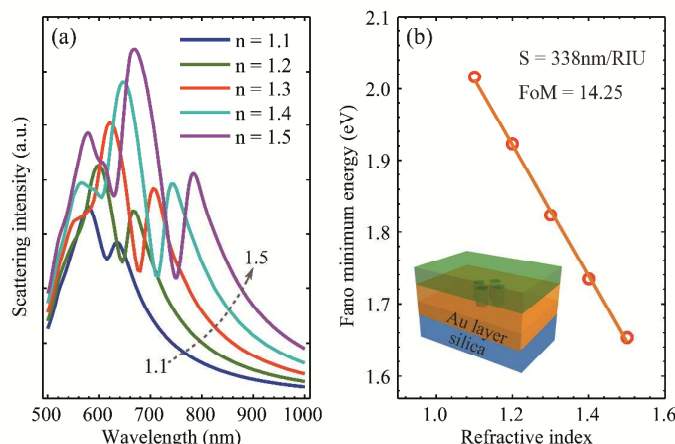


Fig. 9 The same results as that presented in Figure 8 for a system with a 40 nm layer of Au sandwiched between silica and the nanohole.

In the following, we will compare the charge distributions in the nanohole quadrumer with and without the presence of the Au layer in order to understand the physical mechanisms responsible for the improvements in the sensitivity and linewidth as observed in Fig. 9. Without loss of generality, we assume that the system is

immersed in a substance of $n = 1.4$. For the system with the Au layer, we plot the charge distributions at two interfaces, one at the air/nanohole interface and the other at nanohole/Au interface. For the purpose of direct comparison, the scattering spectra for the system with and without the Au layer underneath are plotted

together in the left panel of Fig. 10, in which the main scattering peaks and dips are labelled from (a) to (f) (a-c: 645, 713 and 745 nm; d-f: 688, 765, 813 nm). Here we focus our attention on the Fano dip in the long wavelength region as it has been engineered for sensing detection. As shown in the left panel, the depth of the Fano dip, manifesting the spectral contrast, becomes significantly

shallow with the presence of the Au layer. In the meanwhile, all the scattering peaks and dips blue-shift strongly and the blue-shift amounts for c, b and a decrease monotonically with respect to their counterparts f, e and d, respectively, which directly results in significant narrowing of the spectral linewidth.

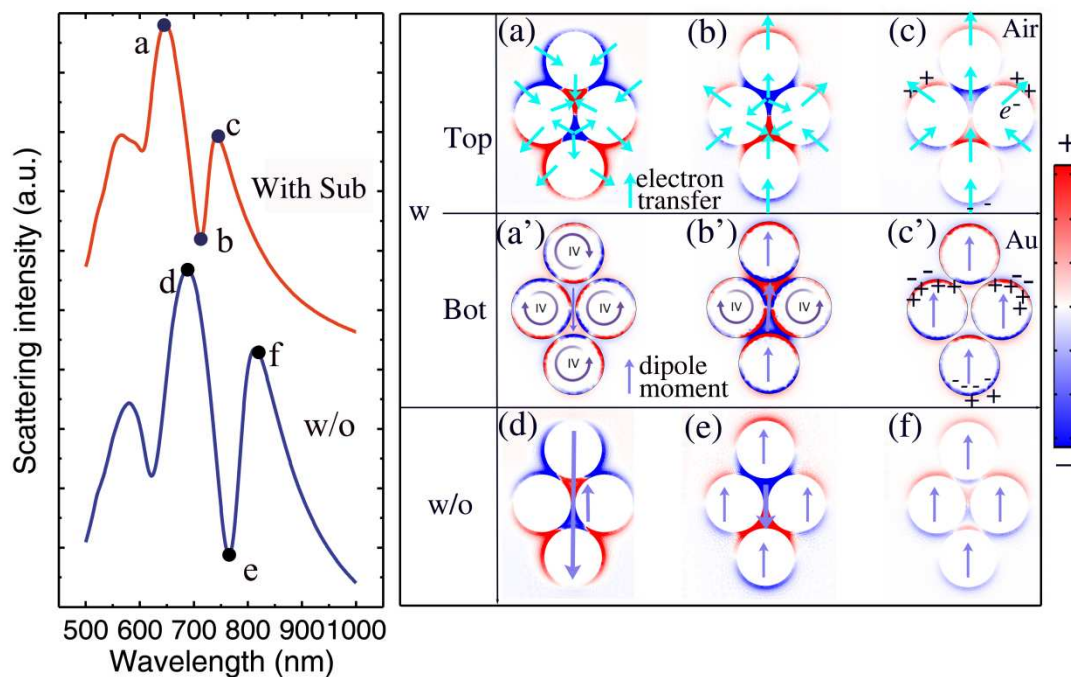


Fig. 10 Left: scattering spectra of the nanohole quadrumer sitting on a conductive Au substrate (red, with sub.) or standing alone in a homogeneous medium (blue, w/o). Right: charge distributions at the top (air/nanohole) and bottom (nanohole/Au) interfaces at the spectral positions a-f indicated in the scattering spectra. Cyan arrows indicate schematically the directions of electron transfer; light-blue arrows show the dipole and quadrupole moments.

The charge density distribution profiles at spectral positions corresponding to (a-f) are plotted in the right panel of Fig. 10. It is found that: 1) the charge distribution at the top interface (air/nanohole) is similar for the system with and without the presence of the Au layer (see the top and bottom panels); 2) the charge distribution at the bottom interface (results not shown) is almost identical to that at the top interface when the Au layer is absent, which is due to the homogenous environment surrounding the system; 3) the charge distribution at the bottom interface alters significantly from that at the top interface when the Au layer is present, with new modes emerging. In the following, we focus on these new modes such as charge transfer plasmon (CTP)⁵⁷ and investigate in detail the electron transfer process and the resultant plasmon modes at the nanohole/Au interface. The cyan arrows in the top panel indicate the direction of electron transfer, showing the moving routes of electrons from the initial states (a-c) towards the steady states (a'-c'). It is worth noting that the distinctive difference between the charge distributions in (a'-c') and (a-c) is that the charges in (a-c) are all resided outside the nanoholes (since there is no free electrons in air), while all the charges in (a'-c') are nearly located inside the nanohole rims. This reveals an intense charge transfer with directions coinciding exactly with the cyan arrows shown in (a-c), i.e., following the Fick's diffusion law. As shown in Fig. 10(a'), the four quadrupolar modes are formed finally when the charges reach the steady state; at this stage, only an extremely-weak dipole at the

centre contributes to the overall dipole moment. The quadrupolar modes can also be found in (b'); however, the net dipole moment becomes much stronger due to the three dipole moments in series. Such a dipolar character of the conductive substrate dominates the whole system at the scattering peak (c), where all modes oscillation in phase. The results suggest that: 1) compared to the system standing alone or on a dielectric substrate like silica, the bright modes can be more easily excited in the high photon-energy region with the presence of a conductive substrate through the assistance of CTP, resulting in a blue-shift in the Fano resonance wavelength;⁵⁷ 2) compared to the charge distributions for the system without the Au layer (i.e., d-f), it can be seen that the original dipolar mode around each nanohole rim changes little at the spectral position c; however, four or two quadrupolar modes emerge at spectral positions a and b, respectively, as shown in (a') and (b'). Such substrate-induced subradiant modes with decreased or reversed net dipole moments reduce the radiative decay-channels and result in a much narrower linewidth with respect to the broad dipolar mode^{5,8,58}. Therefore, mediated by the substrate-induced subradiant modes, the whole bright mode, the subradiant mode and the hybridized Fano dip should all exhibit smaller resonance linewidths than the system standing alone or on the dielectric substrate. In addition, the degradation of the spectral contrast due to the increased scattering intensity at the Fano dip b is simply originated from direct reflection of the incident light by the conductive layer.

3 Conclusion

In conclusion, we have proposed and demonstrated numerically that a nanohole quadrumer supports prominent Fano resonances, which can be engineered effectively by tuning the polarization orientation and geometrical parameters. Our results show that the Fano response is strongest when the incident electric field is polarized along the long-axis of the nanohole cluster. With an exact mathematical treatment, the hybridized scattering spectrum with a Fano lineshape is decomposed quantitatively into the bright and dark modes, revealing intuitively the coherent interference between these modes and the interior physical origin of the pronounced Fano resonance. The profiles of electric field and charge density illustrate the existence of, and interactions between, the dipole, quadrupole and sextupole plasmonic modes. Finally, by properly optimizing the geometric parameters, the nanohole quadrumer supported on a conductive substrate is demonstrated to have an overall sensing FoM value of 14.25, benefitting from both the enhanced sensitivity and the narrowed resonance linewidth. We believe that the proposed nanohole cluster system could be a promising candidate for biochemical sensing applications taking advantage of the pronounced Fano resonance property.

Acknowledgements

X Li and Y Zhan thank the support by the National Natural Science Foundation of China (No. 91233119, No. 61204066), Ph.D. Programs Foundation of Ministry of Education of China (No. 20133201110021), Jiangsu Planned Projects for Postdoctoral Research Funds (No. 1302100B), "Thousand Young Talents Program" of China, and Priority Academic Program Development (PAPD) of Jiangsu Higher Education Institutions. DY Lei acknowledges the support by the Hong Kong Research Grants Council (ECS Grant No. 509513) and the National Natural Science Foundation of China (Grant No. 11304261).

Notes and references

^aInstitute of Modern Optical Technologies & Collaborative Innovation Center of Suzhou Nano Science and Technology, Key Lab of Advanced Optical Manufacturing Technologies of Jiangsu Province & Key Lab of Modern Optical Technologies of Education Ministry of China, Soochow University, Suzhou 215006, China. Corresponding Author: Xiaofeng Li, E-mail: xfli@suda.edu.cn

^bDepartment of Applied Physics, The Hong Kong Polytechnic University, Hong Kong, China. Corresponding Author: Dang Yuan Lei, E-mail: dylei@polyu.edu.hk

^cShenzhen Research Institute, The Hong Kong Polytechnic University, Shenzhen, China.

^dDepartment of Physics, Imperial College London, London SW7 2AZ, United Kingdom.

†These two authors contributed equally to this work.

1 A. N. Poddubny, M. V. Rybin, M. F. Limonov, and Y. S. Kivshar, *Nat Commun*, 2012, **3**, 914.

2 C. Wu, A. B. Khanikaev, R. Adato, N. Arju, A. A. Yanik, H. Altug, and G. Shvets, *Nat Mater*, 2012, **11**, 69–75.

3 F. Monticone, C. Argyropoulos, and A. Alù, *Sci. Rep.*, 2012, **2**, 912.

4 A. Lovera, B. Gallinet, P. Nordlander, and O. J. F. Martin, *ACS Nano*, 2013, **7**, 4527–4536.

5 J. A. Fan, K. Bao, C. Wu, J. Bao, R. Bardhan, N. J. Halas, V. N. Manoharan, G. Shvets, P. Nordlander, and F. Capasso, *Nano Lett.*, 2010, **10**, 4680–4685.

6 U. Fano, *Phys. Rev.*, 1961, **124**, 1866–1878.

7 S. Zhang, L. Chen, Y. Huang, and H. Xu, *Nanoscale*, 2013, **5**, 6985–6991.

8 B. Gallinet and O. J. F. Martin, *ACS Nano*, 2011, **5**, 8999–9008.

9 N. J. Halas, S. Lal, S. Link, W.-S. Chang, D. Natelson, J. H. Hafner, and P. Nordlander, *Adv. Mater.*, 2012, **24**, 4842–4877.

10 E. Prodan, C. Radloff, N. J. Halas, and P. Nordlander, *Science*, 2003, **302**, 419–422.

11 H. Wang, D. W. Brandl, P. Nordlander, and N. J. Halas, *Acc. Chem. Res.*, 2007, **40**, 53–62.

12 N. Liu, S. Mukherjee, K. Bao, Y. Li, L. V. Brown, P. Nordlander, and N. J. Halas, *ACS Nano*, 2012, **6**, 5482–5488.

13 N. Liu, S. Mukherjee, K. Bao, L. V. Brown, J. Dorfmueller, P. Nordlander, and N. J. Halas, *Nano Lett.*, 2012, **12**, 364–369.

14 N. T. Fofang, N. K. Grady, Z. Fan, A. O. Govorov, and N. J. Halas, *Nano Lett.*, 2011, **11**, 1556–1560.

15 D. E. Gómez, Z. Q. Teo, M. Altissimo, T. J. Davis, S. Earl, and A. Roberts, *Nano Lett.*, 2013, **13**, 3722–3728.

16 D. Wu, S. Jiang, Y. Cheng, and X. Liu, *Opt. Express*, 2012, **20**, 26559–26567.

17 T. G. Habteyes, S. Dhuey, S. Cabrini, P. J. Schuck, and S. R. Leone, *Nano Lett.*, 2011, **11**, 1819–1825.

18 N. Verellen, Y. Sonnefraud, H. Sobhani, F. Hao, V. V. Moshchalkov, P. V. Dorpe, P. Nordlander, and S. A. Maier, *Nano Lett.*, 2009, **9**, 1663–1667.

19 Y. Francescato, V. Giannini, and S. A. Maier, *ACS Nano*, 2012, **6**, 1830–1838.

20 A. Artar, A. A. Yanik, and H. Altug, *Nano Lett.*, 2011, **11**, 3694–3700.

21 G. F. Walsh and L. Dal Negro, *Nano Lett.*, 2013, **13**, 3111–3117.

22 R. Near, C. Tabor, J. Duan, R. Pachter, and M. El-Sayed, *Nano Lett.*, 2012, **12**, 2158–2164.

23 S. N. Sheikholeslami, A. Garcia-Etxarri, and J. A. Dionne, *Nano Lett.*, 2011, **11**, 3927–3934.

24 J. A. Fan, Y. He, K. Bao, C. Wu, J. Bao, N. B. Schade, V. N. Manoharan, G. Shvets, P. Nordlander, D. R. Liu, and F. Capasso, *Nano Lett.*, 2011, **11**, 4859–4864.

25 K. Thyagarajan, J. Butet, and O. J. F. Martin, *Nano Lett.*, 2013, **13**, 1847–1851.

26 S.-D. Liu, Y.-B. Yang, Z.-H. Chen, W.-J. Wang, H.-M. Fei, M.-J. Zhang, and Y.-C. Wang, *J. Phys. Chem. C*, 2013, **117**, 14218–14228.

27 Y. Cui, J. Zhou, V. A. Tamma, and W. Park, *ACS Nano*, 2012, **6**, 2385–2393.

28 M. Hentschel, M. Saliba, R. Vogelgesang, H. Giessen, A. P. Alivisatos, and N. Liu, *Nano Lett.*, 2010, **10**, 2721–2726.

29 P. Alonso-Gonzalez, M. Schnell, P. Sarriugarte, H. Sobhani, C. Wu, N. Arju, A. Khanikaev, F. Golmar, P. Albella, L. Arzubiaga, F. Casanova, L. E. Hueso, P. Nordlander, G. Shvets, and R. Hillenbrand, *Nano Lett.*, 2011, **11**, 3922–3926.

30 J. B. Lassiter, H. Sobhani, J. A. Fan, J. Kundu, F. Capasso, P. Nordlander, and N. J. Halas, *Nano Lett.*, 2010, **10**, 3184–3189.

31 Z. Fang, J. Cai, Z. Yan, P. Nordlander, N. J. Halas, and X. Zhu, *Nano Lett.*, 2011, **11**, 4475–4479.

32 W.-S. Chang, J. B. Lassiter, P. Swanglap, H. Sobhani, S. Khatua, P. Nordlander, N. J. Halas, and S. Link, *Nano Lett.*, 2012, **12**, 4977–4982.

33 Z. Fang, Z. Liu, Y. Wang, P. M. Ajayan, P. Nordlander, and N. J. Halas, *Nano Lett.*, 2012, **12**, 3808–3813.

34 J. Ye, F. Wen, H. Sobhani, J. B. Lassiter, P. V. Dorpe, P. Nordlander, and N. J. Halas, *Nano Lett.*, 2012, **12**, 1660–1667.

35 F. Hao, Y. Sonnefraud, P. V. Dorpe, S. A. Maier, N. J. Halas, and P. Nordlander, *Nano Lett.*, 2008, **8**, 3983–3988.

36 J. Henzie, M. H. Lee, and T. W. Odom, *Nat Nano*, 2007, **2**, 549–554.

- 37 Y. Shen, J. Zhou, T. Liu, Y. Tao, R. Jiang, M. Liu, G. Xiao, J. Zhu, Z.-K. Zhou, X. Wang, C. Jin, and J. Wang, *Nat Commun*, 2013, **4**, 2381.
- 38 P. Offermans, M. C. Schaafsma, S. R. K. Rodriguez, Y. Zhang, M. Crego-Calama, S. H. Brongersma, and J. Gómez Rivas, *ACS Nano*, 2011, **5**, 5151–5157.
- 39 K. Lodewijks, W. Van Roy, G. Borghs, L. Lagae, and P. Van Dorpe, *Nano Lett.*, 2012, **12**, 1655–1659.
- 40 F. López-Tejeira, R. Paniagua-Domínguez, and J. A. Sánchez-Gil, *ACS Nano*, 2012, **6**, 8989–8996.
- 41 D. Y. Lei, J. T. K. Wan, and H. C. Ong, *Nanotechnology*, 2012, **23**, 275501.
- 42 M. A. Schmidt, D. Y. Lei, L. Wondraczek, V. Nazabal, and S. A. Maier, *Nat Commun.*, 2012, **3**, 1108.
- 15 43 B. Hopkins, W. Liu, A. E. Miroshnichenko, and Y. S. Kivshar, *Nanoscale*, 2013, **5**, 6395–6403.
- 44 B. Hopkins, A. N. Poddubny, A. E. Miroshnichenko, and Y. S. Kivshar, *Phys. Rev. A*, 2013, **88**, 053819.
- 45 S. Fan, W. Suh, J. D. Joannopoulos, *J. Opt. Soc. Am. A*, 2003, **20**, 569–572.
- 20 46 Z. Ruan, S. Fan *J. Phys. Chem. C*, 2010, **114**, 7324–7329.
- 47 B. Gallinet and O. J. F. Martin, *Phys. Rev. B*, 2011, **83**, 235427.
- 48 J. B. Lassiter, H. Sobhani, M. W. Knight, W. S. Mielczarek, P. Nordlander, and N. J. Halas, *Nano Lett.*, 2012, **12**, 1058–1062.
- 25 49 M. Rahmani, D. Y. Lei, V. Giannini, B. Lukiyanchuk, M. Ranjbar, T. Y. F. Liew, M. Hong, and S. A. Maier, *Nano Lett.*, 2012, **12**, 2101–2106.
- 50 C. Forestiere, L. Dal Negro, and G. Miano, *Phys. Rev. B*, 2013, **88**, 155411.
- 30 51 M. I. Stockman, S. V. Faleev, and D. J. Bergman, *Phys. Rev. Lett.*, 2001, **87**, 167401.
- 52 S. Zhang, K. Bao, N. J. Halas, H. Xu, and P. Nordlander, *Nano Lett.*, 2011, **11**, 1657–1663.
- 53 W. H. Ni, T. Ambjořmsson, S. P. Apell, H. J. Chen, and J. F. Wang, *Nano Lett.*, 2010, **10**, 77–84.
- 35 54 P. B. Johnson and R. W. Christy, *Phys. Rev. B*, 1972, **6**, 4370–4379.
- 55 A. E. Miroshnichenko, S. Flach, and Y. S. Kivshar, *Rev. Mod. Phys.*, 2010, **82**, 2257–2298.
- 56 A. L. Koh, K. Bao, I. Khan, W. E. Smith, G. Kothleitner, P. Nordlander, S. A. Maier, and D. W. McComb, *ACS Nano*, 2009, **3**, 3015–3022.
- 40 57 Y. Wang, Z. Li, K. Zhao, A. Sobhani, X. Zhu, Z. Fang, and N. J. Halas, *Nanoscale*, 2013, **5**, 9897–9901.
- 58 H. Chen, L. Shao, T. Ming, K. C. Woo, Y. C. Man, J. Wang, and H.-Q. Lin, *ACS Nano*, 2011, **5**, 6754–6763.
- 45